University Library

A gateway to Melbourne's research publications

Minerva Access is the Institutional Repository of The University of Melbourne

Author/s:
Shooter, R;Ross, E;Ribal, A;Young, IR;Jonathan, P

Title:
Spatial dependence of extreme seas in the North East Atlantic from satellite altimeter measurements

Date:
2021-06-01

Citation:
Shooter, R., Ross, E., Ribal, A., Young, I. R. & Jonathan, P. (2021). Spatial dependence of extreme seas in the North East Atlantic from satellite altimeter measurements. Environmetrics, 32 (4), https://doi.org/10.1002/env.2674.

Persistent Link:
https://hdl.handle.net/11343/274076

License:
CC BY

Check for updates

Received: 15 July 2020 | Accepted: 16 January 2021

DOI: 10.1002/env.2674

RESEARCH ARTICLE

WILEY

Spatial dependence of extreme seas in the North East Atlantic from satellite altimeter measurements

R. Shooter[1] | **E. Ross**[2] | **A. Ribal**[3] | **I. R. Young**[4] | **P. Jonathan**[5,6]

[1]Met Office Hadley Centre, Exeter, UK

[2]Shell Projects & Technology, Amsterdam, The Netherlands

[3]Department of Mathematics, Faculty of Mathematics and Natural Sciences, Hasanuddin University, Makassar, Indonesia

[4]Department of Infrastructure Engineering, University of Melbourne, Melbourne, Victoria, Australia

[5]Shell Projects & Technology, London, UK

[6]Department of Mathematics and Statistics, Lancaster University, Lancaster, UK

Correspondence
Philip Jonathan, Shell Projects & Technology, London SE1 7NA, UK.
Email: philip.jonathan@shell.com

Abstract

The extremal spatial dependence of significant wave height in the North East Atlantic is explored using Joint Altimetry Satellite Oceanography Network satellite altimeter observations for the period 2002–2018, and a spatial conditional extremes model motivated by the work of Heffernan and Tawn. The analysis involves (a) registering individual satellite passes onto a template transect, (b) marginal extreme value analysis at a set of locations on the template transect and transformation from physical to standard Laplace scale, (c) estimation of the spatial conditional extremes model for a set of locations on a template transect, and (d) comparison of extreme spatial dependence for different template transects. Inferences for two transects considered are qualitatively similar; however, for the "normal ascending" transect running approximately south-west to north-east lying between Iceland and the United Kingdom, extremal spatial dependence is found to decay more quickly than for the second "opposite descending" transect running approximately north-west to south-east to the west of Ireland.

KEYWORDS

altimeter, Atlantic, extreme, satellite, significant wave height, spatial dependence

1 | INTRODUCTION

Simultaneous occurrences of extreme ocean events at different locations can involve considerably higher risk than occurrences of an individual extreme event at one location. For example, resources for evacuating coastal regions or demanning marine facilities can be limited, reducing the efficacy of these approaches to effective risk mitigation. There is interest therefore in characterizing the extremal spatial dependence of severe seas and related phenomena.

Spatial studies of extreme seas typically rely at least to some extent on hindcast data, since sources of large-scale spatial measurements of extreme seas are not available. Previous studies (e.g., Kereszturi et al., 2016; Ross et al., 2017; Shooter et al., 2019; Shooter, Tawn, et al., 2020) based on analysis of hindcast data have shown that the nature and extent of extremal dependence in an ocean basin changes with distance between locations, and also potentially with their relative spatial orientation. In recent years, observations of ocean surface roughness from satellite altimetry have become available, providing a more direct source of data for analysis. In particular, observations along transects of the Joint Altimetry Satellite Oceanography Network (JASON) 1, 2, and 3 satellites along approximately the same longitude–latitude path provide a means to estimate extremal spatial dependence not previously available.

Satellite radar altimeters have been shown to be capable of measuring wind speed and significant wave height to high accuracy (Young et al., 2017; Ribal & Young, 2019). For Earth observation, the combined data record from multiple

This is an open access article under the terms of the Creative Commons Attribution License, which permits use, distribution and reproduction in any medium, provided the original work is properly cited.
© 2021 The Authors. *Environmetrics* published by John Wiley & Sons Ltd.

satellites now spans more than 30 years and has been shown to provide a high-quality data source for global climatology (Young & Donelan, 2018) and extreme value analysis (Takbash et al., 2019; Takbash & Young, 2019). A unique characteristic of altimeter remote sensing is that it provides near-instantaneous measurements over spatial domains (along track) of significant wave height. Hence, the data is suited to investigate the spatial variation of wave properties including extreme values.

In this work, we adopt the spatial conditional extremes model of Shooter et al. (2019), Wadsworth and Tawn (2019) and Shooter, Tawn, et al. (2020), motivated by Heffernan and Tawn (2004), to estimate extremal spatial dependence of significant wave height along satellite transects. This model admits different classes of extremal dependence and is computationally rather straightforward to estimate; it is essentially a nonlinear regression model. Other statistical approaches to spatial extremes are motivated by the theory of max-stable processes (MSPs, see e.g., Brown & Resnick, 1977; Smith, 1990; Schlather, 2002; Davison et al., 2012; Ribatet, 2013; Tawn et al., 2018). However, typical MSP models require an assumption that the extremal spatial dependence takes a particular form (known as "asymptotic dependence," see Section 3); in general, this assumption is unlikely to be appropriate for characterization of severe ocean environments on large spatial domains. Inverted MSP models are available, but these require the assumption that asymptotic dependence is not present. Other asymptotically dependent spatial extremes models have been proposed (e.g., Reich & Shaby, 2012, Ferreira & de Haan, 2014, de Fondeville & Davison, 2018). Some models in principle are able to describe different classes of extremal dependence (e.g., Wadsworth & Tawn, 2012, Wadsworth et al., 2017, Huser & Wadsworth, 2019) but in reality are unrealistically restrictive (e.g., in that only one of asymptotic dependence or asymptotic independence can be present at all distances) or computationally unwieldy.

1.1 | Objectives and outline

The variable of interest in this work is significant wave height (henceforth H_S), a measure of the roughness of the ocean surface at a specific time and location. H_S can be estimated as four times the standard deviation (SD) of the ocean surface over an interval of observation of the order of 1 h. H_S varies slowly in space (over tens of kilometres) and in time (over hours). The objective of the current work is to apply the spatial conditional extremes model to quantify the extremal spatial dependence of significant wave height in the North East Atlantic as measured by the satellite altimetry.

The layout of the paper is as follows. Section 2 introduces the JASON altimeter data, and describes the preprocessing of data necessary in advance of extreme value modeling. The spatial conditional extremes model is described in Section 3. Results of applying the spatial conditional extremes model for two North East Atlantic transects are then given in Section 4. Section 5 provides discussion and conclusions. Software, data, and supporting results are provided in a GitHub repository (Shooter, Ross, & Jonathan, 2020).

2 | DATA

2.1 | JASON satellite altimeter missions

JASON 1, 2 and 3 altimeter measurements of the ocean's surface are used in this work. JASON-1 was the successor altimeter mission to TOPEX/Poseidon, which measured ocean surface topography from 1992 to 2005. Like its predecessor, JASON-1 was a joint project between NASA and the French space agency CNES. JASON-1 was launched in December 2001 and decommissioned in June 2013. In the initial calibration phase of follow-up mission JASON-2 (launched in June 2008), both JASON-1 and JASON-2 satellites were placed in the same track and phased approximately 56 s apart. However, the JASON-1 orbit started to drift in January 2009. After approximately 11 years of operation, JASON-2 was decommissioned in October 2019. To ensure continuity of high-quality measurements for ocean science applications, JASON-3 was launched in January 2016 and is still operational. All three JASON missions were placed in near-polar orbits, covering the globe from latitude 66°S to 66°N. The exact repeated mission, inclination, and altitude for all satellites were 10 days, 66° and 1336 km. The altimeters on all three JASON satellites were similar, with dual systems using separate antennas operating in the Ku-band (13.575 GHz) and C-band (5.3 GHz).

All H_S data measured by JASON-1, JASON-2, and JASON-3 were sourced from the Australian Ocean Data Network. These datasets have been calibrated and quality controlled as described by Ribal and Young (2019). The database is updated every 6 months and presently includes data up to the end of June 2020. Each along-track measurement is allocated a data quality flag designating an observation as one of "good," "probably good," "bad," and "missing." The

TABLE 1 Description of the JASON transects considered. "SWNE" refers to the normal ascending transect. "NWSE" refers to the opposite descending transect

Altimeter	Transect	Start date (UTC)	End date (UTC)	Number of transects used
JASON-1	SWNE	January 15, 2002 17:14:52	June 20, 2013 04:40:28	888
JASON-2	SWNE	July 4,2008 14:13:15	July 16, 2018 10:02:12	696
JASON-3	SWNE	February 12, 2016 22:33:12	July 16, 2018 09:17:51	155
JASON-1	NWSE	January 15, 2002 21:08:22	June 19, 2013 10:11:39	885
JASON-2	NWSE	July 5, 2008 20:28:01	July 13, 2018 17:02:20	693
JASON-3	NWSE	February 14, 2016 04:48:27	July 15, 2018 16:44:11	158

present analysis uses "good" data only. The analysis of Ribal and Young (2019) calibrated altimeter measurements against U.S. National Data Buoy Centre (NDBC) buoy data, applying a linear regression correction to the raw H_S data from the missions. In addition, the validation analysis conducted by Ribal and Young (2019) investigated the performance of the altimeters at extreme H_S up to 9 m. The analysis showed no indication of degradation of the signals at these extreme values.

The altimeter tracks from JASON-1, JASON-2, and JASON-3 used in the current study were selected from an area bounded by longitudes from 330°E to 360°E, and latitudes from 45°N to 65°N. Two specific transects were used in the analysis. The "normal" transect (also referred to as "SWNE") is an ascending south-west to north-east track whereas the "opposite" transect (also "NWSE") descends from north-west to south-east. Due to orbital drift, the tracks for JASON-1 and JASON-2 vary spatially whereas the track of JASON-3 is more stable. The duration of the available data from each satellite is summarized in Table 1, together with the numbers of transects available for analysis.

2.2 | Transect registration and marginal transformation

We estimate extremal spatial dependence for a small set of p "registration locations" $r_R(j), j = 0, 1, \ldots, q$ on a template transect, where $p = q + 1$. We define registration locations as shown in Figure 1. These are approximately equidistant between adjacent JASON-3 transects and approximately equally spaced in the transect direction, for the SWNE and NWSE tracks. For each available satellite pass $r_\ell(t)$, $t \in$ time period T_ℓ, and pass index $\ell = 1, 2, \ldots$ over the region of interest, we find the nearest point $r_\ell(t_j^*)$ on the satellite transect to each of the p registration locations $r_R(j), j = 0, 1, \ldots, q$ such that

$$t_j^* = \underset{t \in T_\ell}{\operatorname{argmin}} \ \operatorname{dist}(r_\ell(t), r_R(j)), \tag{1}$$

with physical distance dist calculated using the spherical law of cosines, and allocate the value of H_S measured at $r_\ell(t_j^*)$ to $r_R(j)$. Further, denote the minimum distance $\operatorname{dist}(r_\ell(t_j^*), r_R(j))$ by $r_{\ell j}$. For any satellite pass ℓ, if the maximum of $r_{\ell j}$ exceeds 50 km the pass is not registered. In this way, we obtain "registered transects" for each pass of JASON 1, 2, and 3 over the region of interest, and a sequence of p measurements of H_S at the registration locations for each transect. The total number of transects included is 691, 581, and 125 for each of JASON 1, 2 and 3 for the SWNE track, and 588, 559, and 127 for the NWSE track. Figure 1 shows $p = 19$ registration locations for each transect, the first of which (location 0) is referred to as the "reference location" or "conditioning location."

The prevailing wind and storm direction in this mid-latitude region is from the south-west or west. The SWNE transect therefore is typically more aligned with the direction of storm propagation, whereas the NWSE transect lies approximately perpendicular to it, and therefore approximately parallel to the region of highest H_S (e.g., Young, 2017). H_S on the SWNE transect is also more likely to be influenced by the presence of the UK and Icelandic land masses.

Scatter plots of H_S from subsets of locations on the SWNE and NWSE tracks are shown in Figures 2 and 3. We see that the dependence between H_S at different locations decreases with distance between locations. However there is a positive association between H_S values even when locations are separated by more than 1000 km. It appears that the strength of dependence between locations with given separation does not vary obviously along the transect.

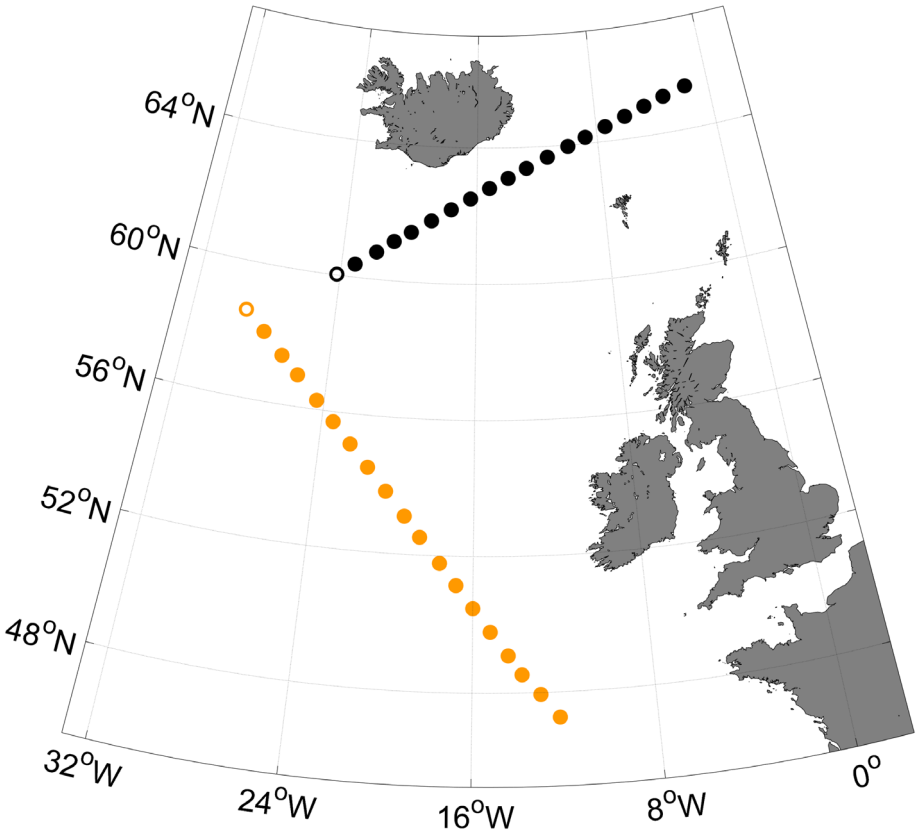

FIGURE 1 Locations of registered satellite measurements on two template transects. Normal ascending SWNE (black) and opposite descending NWSE (orange) transects shown. "Registration locations" are numbered 0,1,2, … ,18 for each transect. The first registration location, referred to as the "reference location," "conditioning location," or "location 0" for the transect, is shown as a hollow disc. Other locations are referred to as "remote locations", show as solid discs

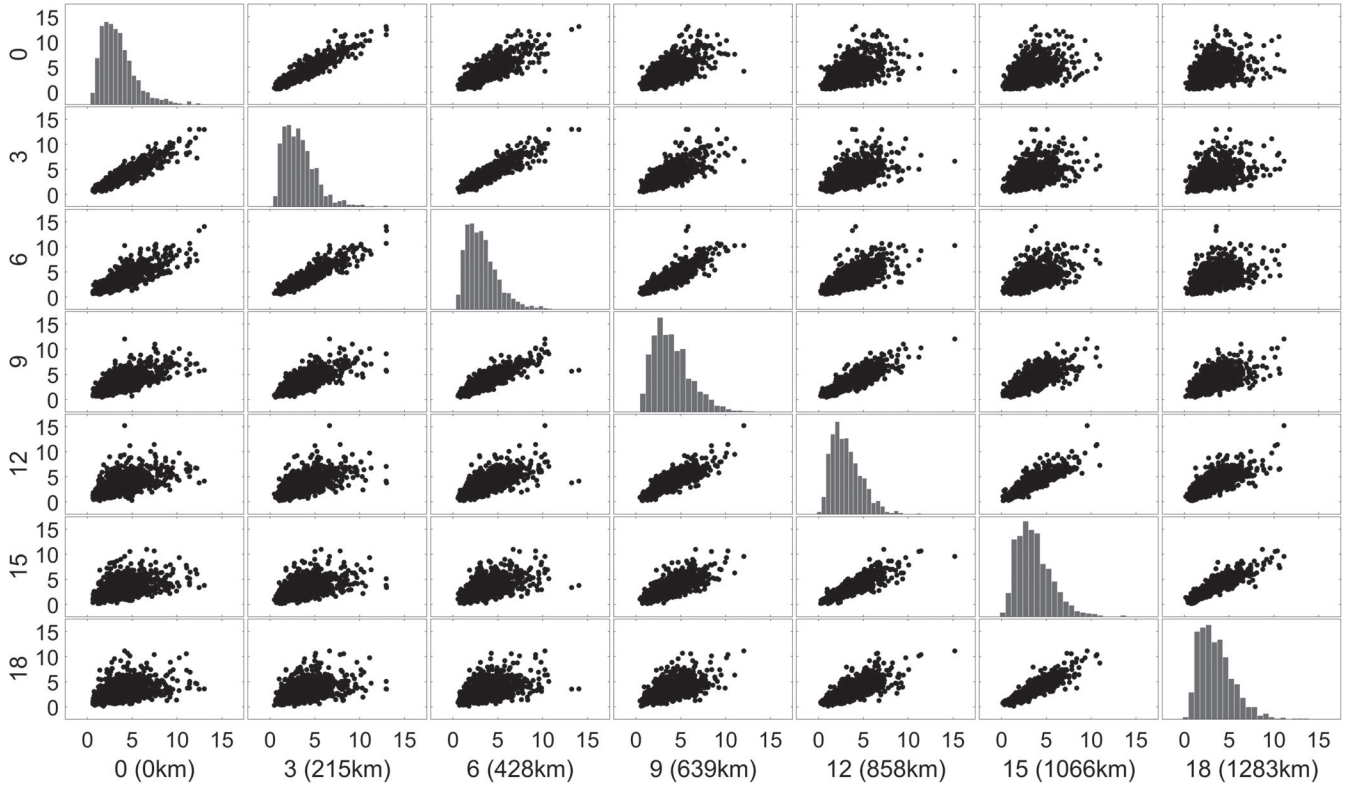

FIGURE 2 Histograms and scatter plots of H_S measurements for the normal ascending transect, on physical scale. Outer axis labels indicate locations (only data for locations 0, 3, 6, … , 18 are shown). Distances from reference location (in km) given in the outer x-axis labels. Inner axis labels are value of H_S (in m)

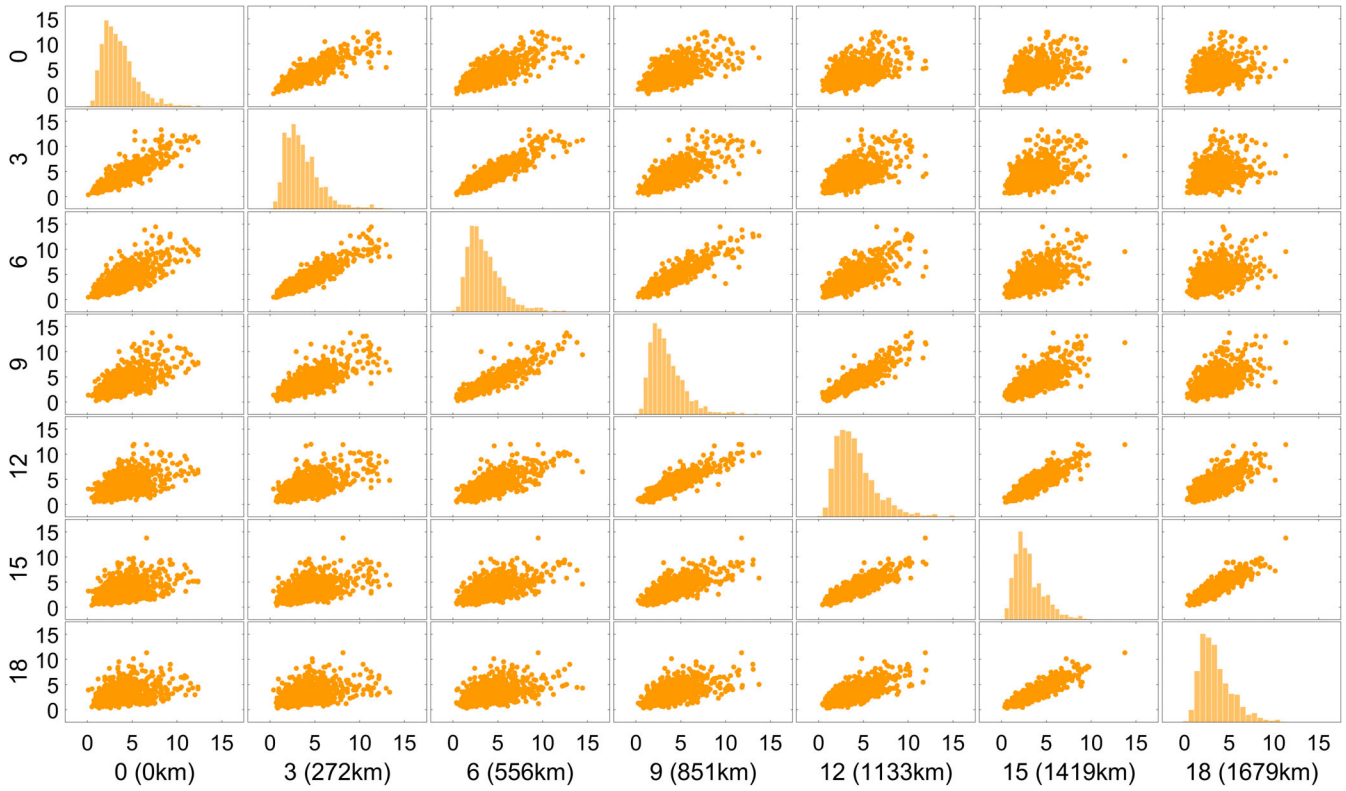

FIGURE 3 Histograms and scatter plots of H_S measurements for the opposite descending transect, on physical scale. Outer axis labels indicate locations (only data for locations 0, 3, 6, … , 18 are shown). Distances from reference location (in km) given in the outer x-axis labels. Inner axis labels are value of H_S (in m)

Marginal extreme value analysis was performed independently for sample data for each of the $2p$ registration locations, and samples thereby transformed to marginal Laplace scale with $\dot{X}$ representing H_S at a location on physical scale. A generalized Pareto (GP) distribution with shape ξ, scale σ and high threshold ψ was fitted to the sample at each registration location. The GP (conditional) cumulative distribution function is $F_{\dot{X}|\dot{X}>\psi}(\dot{x};\xi,\sigma,\psi) = 1-(1+(\xi/\sigma)(\dot{x}-\psi))_+^{-1/\xi}$ for $\dot{x}>\psi$, $\psi\in(-\infty,\infty)$, $\xi\in(-\infty,\infty)\backslash\{0\}$, $\sigma\in(0,\infty)$ and $(y)_+ = y$ for $y>0$ and $=0$ otherwise. When $\xi=0$, the conditional distribution takes the form $1-\exp[-(x-\psi)/\sigma)]$. The sensitivity of estimated ξ to choice of threshold ψ was found to be small for ψ corresponding to the GP quantiles with nonexceedance probabilities τ around 0.7. Marginal analysis suggests that there is some spatial non-stationarity in H_S. To illustrate this, Figure 4 gives 100-year return value estimates (as bootstrap median and 95% uncertainty bands) for the SWNE and NWSE tracks. The T-year return value is the quantile of the annual distribution of a quantity (H_S here) with nonexceedance probability $1-1/T$.

It is interesting that the maximum value of H_S ever reported by buoy measurement is approximately 19 m, recorded at the location of UK Met Office buoy K5 at approximately 59°N, 12°W in 2013 (WMO, N.D.), near to the start of the SWNE track. The unconditional cumulative distribution function $F_{\dot{X}}$ of H_S at a location is then given by $F_{\dot{X}}(\dot{x}) = \tilde{F}_{\dot{X}}(\dot{x})$ if $\dot{x}\le\psi$ and $(1-\tau)F_{\dot{X}|\dot{X}>\psi}(\dot{x})$ otherwise, where $\tilde{F}_{\dot{X}}$ is an empirical ("counting") estimate for the cumulative distribution of threshold nonexceedances. Marginal transformation to Laplace-scale variate X is achieved at each registration location using $F_X(x) = F_{\dot{X}}(\dot{x})$ for $x,\dot{x}\in\mathbb{R}$, where F_X is the cumulative distribution function of the standard Laplace distribution, given by $F_X(x) = (1/2)\exp(x)$ if $x\le 0$ and $1-(1/2)\exp(-x)$ otherwise.

Figures 5 and 6 show scatter plots of threshold exceedances of Laplace-scale H_S at a selection of remote locations on H_S at the reference location for each of the SWNE and NWSE tracks. The threshold level used at the reference location corresponds to the quantile of the Laplace distribution with nonexceedance probability 0.7. Both figures show that dependence between Laplace-scale H_S reduces with increasing distance. For small distances, the dependence is high with data lying approximately on the line $y=x$. At the very largest distances, there is also evidence for a small level of positive dependence. We would expect the estimated spatial conditional extremes model to reflect these features.

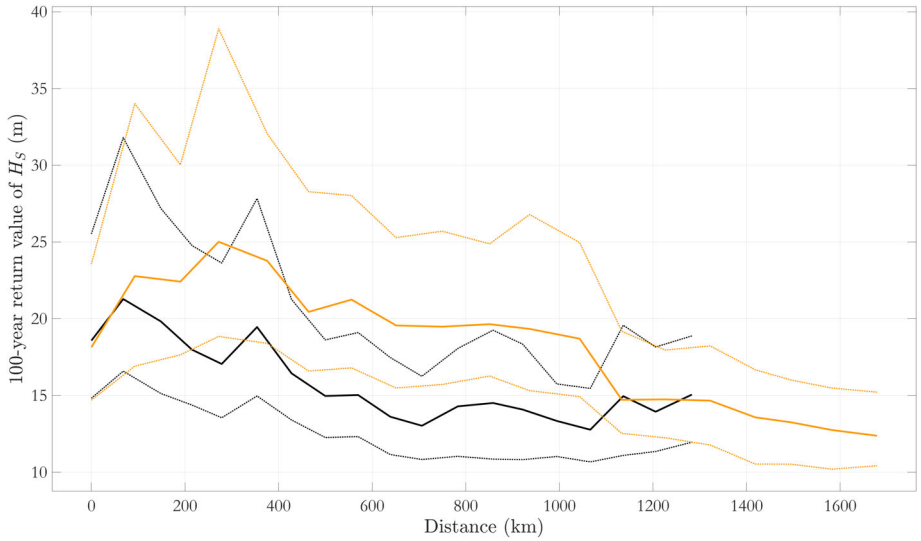

FIGURE 4 Marginal 100-year return value (m) of H_S for normal ascending (black) and opposite descending (orange) transects as a function of distance from reference location, in terms of bootstrap median (solid) and bootstrap 95% uncertainty interval (dotted)

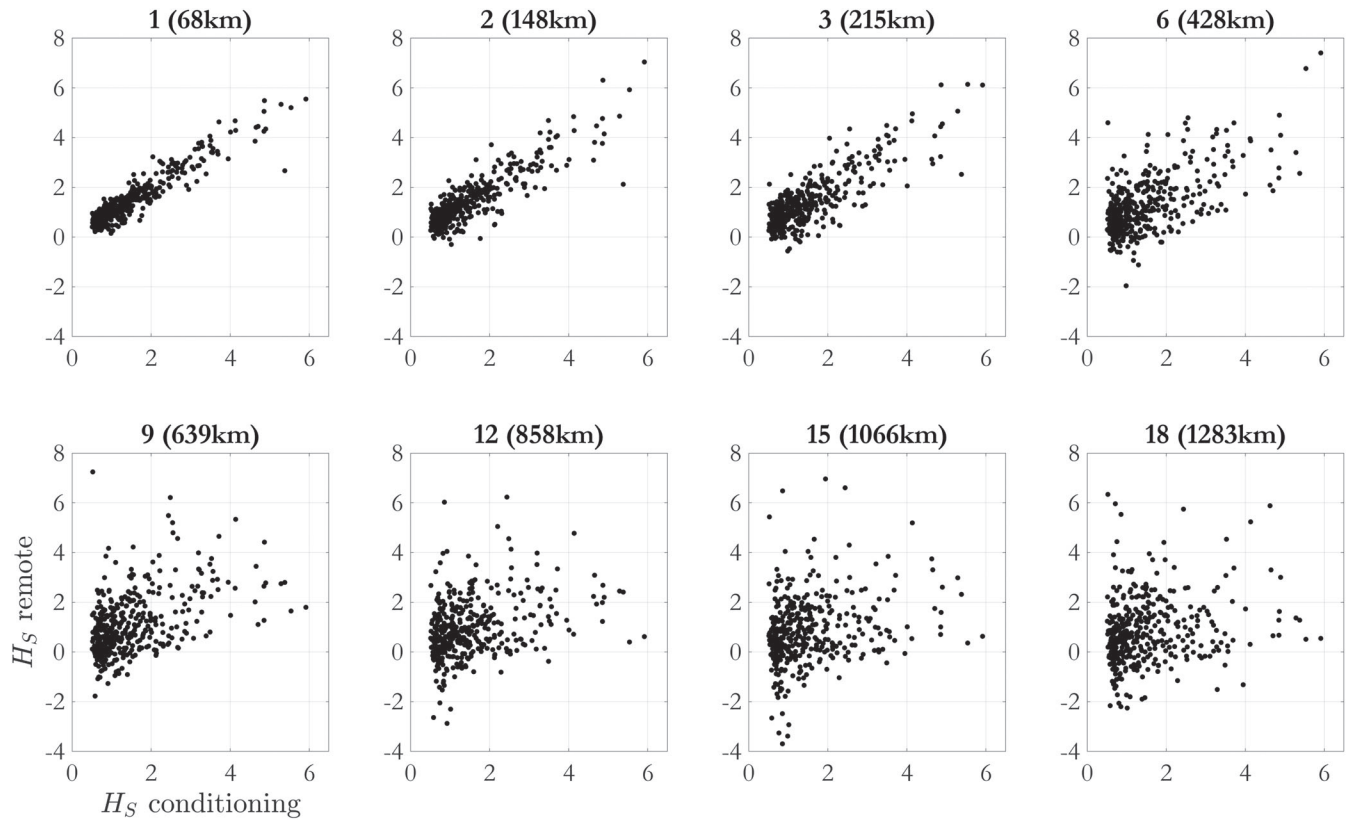

FIGURE 5 Scatter plots of Laplace-scale H_S data for normal ascending transect. Plot of H_S at remote location (y-axis) on H_S at conditioning location (location 0, x-axis) for remote locations 1, 2, 3, 6, 9, 12, 15, and 18 (indicated by panel titles)

3 | MODEL AND INFERENCE

3.1 | Extremal spatial dependence

Severe wind–sea conditions in the North East Atlantic are generated by relatively large-scale atmospheric low pressure systems. Hence for two nearby locations, an extreme value of H_S observed at one location might be expected to be associated with an extreme observation at another. Extremes observed at distant pairs of locations are less likely to be related.

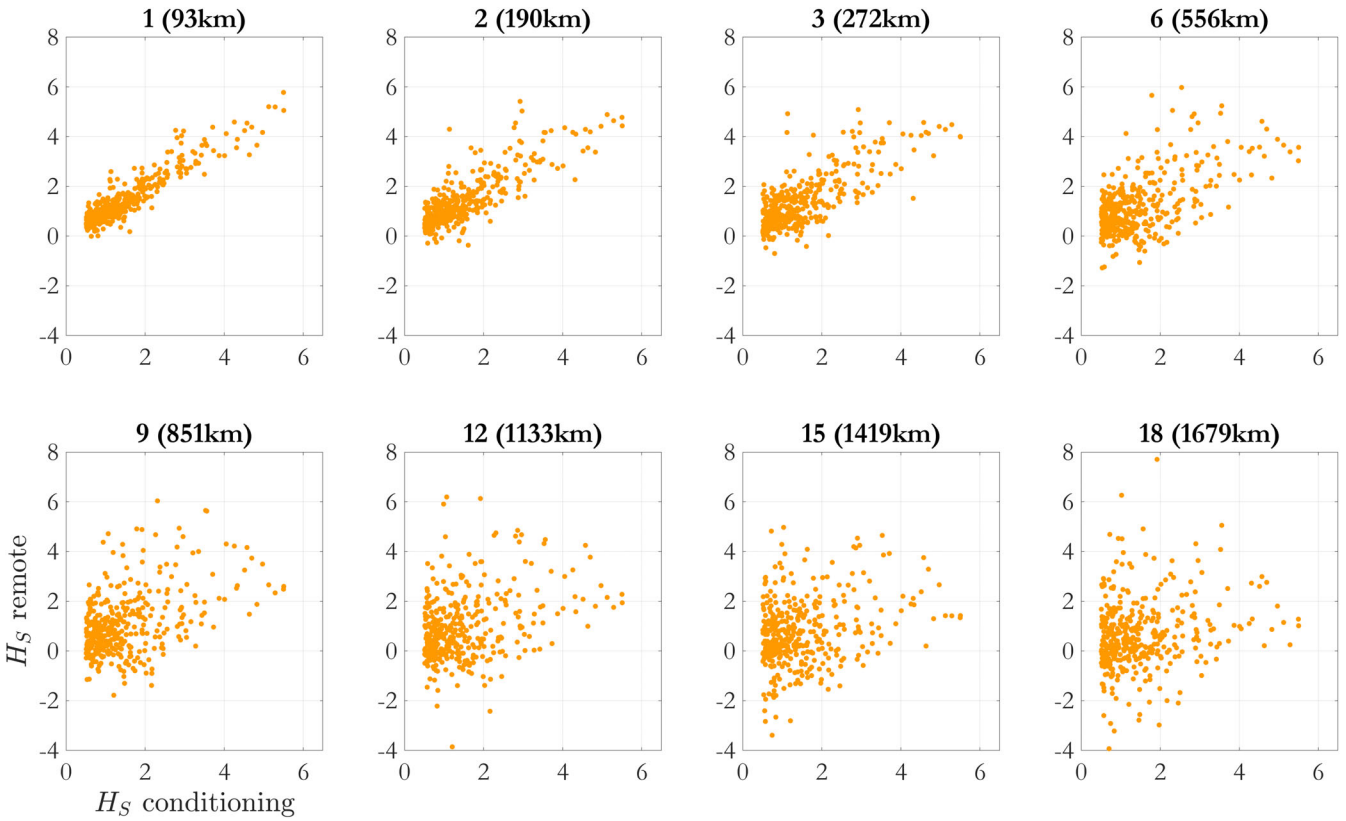

FIGURE 6 Scatter plots of Laplace-scale H_S data for opposite descending transect. Plot of H_S at remote location (y-axis) on H_S at conditioning location (location 0, x-axis) for remote locations 1, 2, 3, 6, 9, 12, 15, and 18 (indicated by panel titles)

We can calculate the probability that given an observation of an extreme event at one location, we observe extreme events simultaneously at other locations, providing a measure of dependence between the events. Coles et al. (1999) introduce the measures χ and $\overline{\chi}$, estimated via their subasymptotic forms $\chi(u)$ and $\overline{\chi}(u)$, where $u \in [0,1]$, to describe extremal dependence. For bivariate uniform random variables (U, V) these are defined as $\chi(u) = 2 - \log \mathbb{P}(U < u, V < v)/\log \mathbb{P}(U < u)$ and $\overline{\chi}(u) = 2\log \mathbb{P}(U > u)/\log \mathbb{P}(U > u, V > v) - 1$. χ and $\overline{\chi}$ may be obtained by taking the respective limits of these functions, as $u \to 1$. The nature of extremal dependence between U and V may then be classified by considering χ and $\overline{\chi}$ together. If $\chi = 0$ and $-1 \leq \overline{\chi} < 1$, the random variables are asymptotically independent (AI), and the value of $\overline{\chi}$ signifies the level of dependence. On the other hand, if $\overline{\chi} = 1$ and $0 < \chi \leq 1$, then the pair (U, V) exhibit asymptotic dependence (AD), with χ providing a measure of this. See Ledford and Tawn (1996), Coles et al. (1999), and Tawn et al. (2018) for further details.

3.2 | Multivariate conditional extremes

Suppose now we have a vector of random variables $(X_0, \mathbf{X})$, where X_0 and $\mathbf{X} = (X_1, \ldots, X_q)$ temporarily have Gumbel marginal distributions, and random variables $\mathbf{Z} = (\mathbf{X} - \mathbf{a}(X_0))/\mathbf{b}(X_0)$ for functions $\mathbf{a} : \mathbb{R} \to \mathbb{R}^q$ and $\mathbf{b} : \mathbb{R} \to \mathbb{R}^q$, where all operations are taken to be component-wise. Heffernan and Tawn (2004) assume the existence of $\mathbf{a}$ and $\mathbf{b}$ such that, for $x > 0$, $\lim_{u\to\infty} \mathbb{P}(\mathbf{Z} \leq \mathbf{z}, X_0 - u > x | X_0 > u) = G(\mathbf{z})\exp(-x)$, where G is a joint distribution with nondegenerate margins; asymptotic justification is given by Heffernan and Tawn (2004) and Heffernan and Resnick (2007). Keef et al. (2013) show that if $(X_0, \mathbf{X})$ has Laplace-distributed margins then canonical functional forms for $\mathbf{a}(\cdot)$ and $\mathbf{b}(\cdot)$ are $\mathbf{a}(x) = \boldsymbol{\alpha} x$ and $\mathbf{b}(x) = x^{\boldsymbol{\beta}}$ (for $x > 0$), where $\boldsymbol{\alpha} = (\alpha_1, \alpha_2, \ldots, \alpha_q)$ and $\boldsymbol{\beta} = (\beta_1, \beta_2, \ldots, \beta_q)$, and $\alpha_j \in [-1, 1]$ and $\beta_j \in (-\infty, 1]$. We assume positive dependence, restricting $\alpha_j \in [0, 1]$, $\beta_j \in [0, 1]$ for all "remote locations" $j \in \{1, 2, \ldots, q\}$. For some high threshold u and all $x_0 > u$, we assume the model form $\mathbf{X} | \{X_0 = x_0\} = \boldsymbol{\alpha} x_0 + x_0^{\boldsymbol{\beta}} \mathbf{Z}$, where $\mathbf{Z} \sim G$ is independent of X_0. Different values for (α_j, β_j) indicate different classes of extremal dependence as follows: $(\alpha_j, \beta_j) = (1, 0)$ corresponds to AD, $\alpha_j = 0$ to perfect

independence, and intermediate values of α_j to AI. Thus, on Laplace scale, for positive dependence: (a) AD corresponds to X_j and X_0 for large X_0 growing at the same rate with conditional extremes slope parameter $\alpha_j = 1$, $\beta_j = 0$, (b) AI corresponds to X_j growing more slowly than X_0, with $\alpha_j \in (0, 1)$, and (c) perfect independence corresponds to X_j not growing with X_0, and $\alpha_j = 0$.

3.3 | Spatial conditional extremes

We extend the multivariate conditional extremes model outlined in Section 3.2 to a spatial context using the spatial conditional extremes (SCE) model described by Tawn et al. (2018), Wadsworth and Tawn (2019) and Shooter, Tawn, et al. (2020). Specifically, we represent H_S on the SWNE and NWSE transects by spatial process $X(\cdot)$ on domain S with Laplace marginal distributions. Then for distance $d \in \mathbb{R}_{\geq 0}$ between locations $r, r' \in S$, with positive dependence between variables, for all $x_0 > u$, $X(r')|\{X(r) = x_0\} = \alpha(d)x_0 + x_0^{\beta(d)} Z(r' - r)$, where $\alpha : \mathbb{R}_{>0} \to [0, 1]$, $\beta : \mathbb{R}_{>0} \to [0, 1]$ and $Z(\cdot)$ is a residual process independent of $X(\cdot)$. To make inferences using vector $\mathbf{X}$ of random variables observed at registration locations $\{r_R(j)\}_{j=0}^{q}$, $X(\cdot)$ is treated as finite-dimensional. We set $d_j = \text{dist}(r_R(j), r_R(0))$ for $j = 1, 2, \ldots, q$ for distance $\text{dist}(\cdot, \cdot)$ between locations, $\alpha_j = \alpha(d_j)$ and $\beta_j = \beta(d_j)$. We assume that $Z(\cdot)$ has delta-Laplace (or generalized Gaussian) margins with parameters μ, σ and δ dependent on d, which need to be estimated. The marginal density f_{Z_j} of Z at distance d_j is

$$f_{Z_j}(z_j) = \frac{\delta_j}{2\kappa_j \sigma_j \Gamma\left(\frac{1}{\delta_j}\right)} \exp\left\{ -\left| \frac{z - \mu_j}{\kappa_j \sigma_j} \right|^{\delta_j} \right\}, \tag{2}$$

for $j = 1, 2, \ldots, q$, $\delta_j, \sigma_j, \kappa_j \in \mathbb{R}_{>0}$, $\mu_j \in \mathbb{R}$, $z_j \in \mathbb{R}$, where $\kappa_j^2 = \Gamma\left(1/\delta_j\right) / \Gamma\left(3/\delta_j\right)$ and $\Gamma(\cdot)$ represents the gamma function. The mean and variance of this distribution are, respectively, μ_j and σ_j^2, regardless of the choice of δ_j, and the distribution is henceforth denoted by $\text{DL}(\mu_j, \sigma_j^2, \delta_j)$. The case $\delta_j = 2$ corresponds to a Gaussian distribution, and $\delta_j = 1$ to a Laplace distribution; the standard Laplace distribution with variance 2 corresponds to $\sigma_j^2 = 2$ in our notation. As $d \to \infty$, we approach perfect independence between locations with $\mu_j \to 0$, and $\delta_j \to 1$, $\sigma_j \to \sqrt{2}$ (i.e. standard Laplace), and also $\alpha_j, \beta_j \to 0$. The model is not informative for δ_j at $d = 0$.

Now consider the vector $\mathbf{X}$ corresponding to $p = q + 1$ registration locations with standard Laplace marginal distributions $X_j \sim \text{DL}(0, 2, 1)$ for $j = 0, \ldots, q$. We assume, conditional on $X_0 = x_0$, for $x_0 > u$, that $(X_1, \ldots, X_q)|\{X_0 = x_0\} = \boldsymbol{\alpha} x_0 + x_0^{\boldsymbol{\beta}} \mathbf{Z}$ where $\mathbf{Z} \sim \text{DL}_q(\boldsymbol{\mu}, \boldsymbol{\sigma}^2, \boldsymbol{\delta}; \boldsymbol{\Sigma})$. $\boldsymbol{\Sigma}$ is the $q \times q$ correlation matrix for a Gaussian dependence structure between residual components, and

$$F_{\mathbf{Z}}(\mathbf{z}) = \Phi_q\left(\Phi^{-1}(F_{Z_1}(z_1)), \Phi^{-1}(F_{Z_2}(z_2)), \ldots, \Phi^{-1}(F_{Z_q}(z_q)); \mathbf{0}, \boldsymbol{\Sigma} \right), \tag{3}$$

where F represents a cumulative distribution function and Φ is the cumulative distribution function of a standard Gaussian distribution. $\Phi_q(\mathbf{0}, \boldsymbol{\Sigma})$ is the cumulative distribution function of a q-dimensional Gaussian distribution with mean $\mathbf{0}$ and covariance matrix $\boldsymbol{\Sigma}$. The j, j' element $\Sigma_{jj'}$ of residual correlation matrix $\boldsymbol{\Sigma}$, $j, j' = 1, 2, \ldots, q$ quantifies the dependence between SCE residuals (on standard Gaussian-scale) at registration locations $r_R(j)$ and $r_R(j')$ given conditioning on location $r_R(0)$. Based on the findings of Shooter, Tawn, et al. (2020), we expect that the value of $\Sigma_{jj'}$ depends on both the distance $\text{dist}(r_R(j), r_R(j'))$ between remote locations and distances $\text{dist}(r_R(j), r_R(0))$, $\text{dist}(r_R(j'), r_R(0))$ from remote locations to conditioning site. When $\text{dist}(r_R(j), r_R(0))$ and $\text{dist}(r_R(j'), r_R(0))$ are large relative to $\text{dist}(r_R(j), r_R(j'))$, the conditional correlation between remote locations will be similar to the unconditional correlation. Otherwise we expect conditioning of $r_R(0)$ to influence correlation between process at $r_R(j)$ and $r_R(j')$. We therefore adopt a parameterization for $\boldsymbol{\Sigma}$ equivalent to the correlation function for a standard Gaussian field evaluated at $p = q + 1$ locations conditioned on its value at one location, with powered exponential dependence. With $\boldsymbol{\Sigma}^*$ representing the $p \times p$ correlation matrix of the unconditioned field (and matrix indexing starting from zero for convenience), the correlation matrix $\boldsymbol{\Sigma}$ for the conditional field has elements given by $\Sigma_{jj'} = (\Sigma^*_{jj'} - \Sigma^*_{j0}\Sigma^*_{j'0})(1 - \Sigma^{*2}_{j0})^{-1/2}(1 - \Sigma^{*2}_{j'0})^{-1/2}$ for $j, j' = 1, 2, \ldots, q$ with conditioning location indexed by zero. Further, we assume that the correlation between observations at different locations in the unconstrained field reduces as a function of the distance between locations, with powered exponential form $\Sigma^*_{jj'} = \exp[-(\text{dist}(r_R(j), r_R(j'))/\rho_1)^{\rho_2}]$ for $\rho_1, \rho_2 \in \mathbb{R}_{>0}$ and $j, j' = 0, 1, 2, \ldots, q$, for parameters ρ_1 and ρ_2 to be estimated.

Marginally, writing X_j^c to represent $X_j|\{X_0 = x_0\}$, $j = 1, 2, \ldots, q$, we have $X_j^c = \alpha_j x_0 + x_0^{\beta_j} Z_j \sim \mathrm{DL}(m_j, s_j^2, \delta_j)$, where $Z_j \sim \mathrm{DL}(\mu_j, \sigma_j^2, \delta_j)$ for $j = 1, 2, \ldots, q$, so that $Z_j = Z_j^* \sigma_j + \mu_j$, where $Z_j^* \sim \mathrm{DL}(0, 1, \delta_j)$. Conditional means m_j and standard deviations s_j are given by

$$m_j = \alpha_j x_0 + x_0^{\beta_j} \mu_j \quad \text{and} \quad s_j = x_0^{\beta_j} \sigma_j. \tag{4}$$

Hence

$$\mathbf{X}^c = (\mathbf{X}|\{X_0 = x_0\}) \sim \mathrm{DL}_p(\mathbf{m}, \mathbf{s}^2, \boldsymbol{\delta}; \boldsymbol{\Sigma}) \tag{5}$$

for $x_0 > u$, a q-dimensional delta-Laplace distribution with mean $\mathbf{m} = \{m_j\}_{j=1}^q$, variance $\mathbf{s}^2 = \{s_j^2\}_{j=1}^q$, delta parameters $\boldsymbol{\delta} = \{\delta_j\}_{j=1}^q$ and (standard Gaussian-scale) covariance $\boldsymbol{\Sigma}$.

Given a large value of a random variable at the conditioning location, the SCE model thus describes the dependence between values across the full set of locations in two ways. The relationship between the value at each individual remote location and that at the conditioning location is characterized as a function of the distance between the remote and conditioning locations, using the conditional extremes model. The dependence between values at pairs of remote locations is also characterized (using a Gaussian process after variable transformation) as a function of the distance between those remote locations.

3.4 | Inference

We use Bayesian inference to estimate the joint posterior distribution of the SCE model parameters $\Omega = \{\{\alpha_j, \beta_j, \mu_j, \sigma_j, \delta_j\}_{j=1}^q, \rho_1, \rho_2\}$. To achieve this, we need to derive the sample likelihood for the SCE model, and make a reasonable prior specification for Ω. The description in Section 3.3 is sufficient to evaluate the likelihood for a sample of observations from the registration locations on the SWNE and NWSE transects. As detailed in Shooter, Tawn, et al. (2020), we differentiate Equation (3) to find the joint density function of residuals, and hence using Equation (5) we find the density $f_{\mathbf{X}^c}(\mathbf{x})$ for any observation $\mathbf{x}$ over the p locations. For (Laplace-scale) sample $\{x_{ij}\}_{i=1,j=0}^{n,p}$, the negative log-likelihood is

$$\begin{aligned} &\frac{np}{2}\log(2\pi) + \frac{n}{2}\log|\boldsymbol{\Sigma}| + \sum_{j=1}^{p}\log\left(2s_j\kappa_j\Gamma\left[\frac{1}{\delta_j}\right]\right) - n\sum_{j=1}^{p}\log\delta_j \\ &+ \sum_{i=1}^{n}\left\{\mathbf{w}_i'\boldsymbol{\Sigma}^{-1}\mathbf{w}_i + \sum_{j=1}^{p}\left|\frac{x_{ij}-m_j}{\kappa_j s_j}\right|^{\delta_j} + \sum_{j=1}^{p}\log\phi(w_{ij})\right\}, \end{aligned} \tag{6}$$

where $\kappa_j^2 = \Gamma(1/\delta_j)/\Gamma(3/\delta_j)$ for each j and $\mathbf{w}_i' = (w_{i1}, w_{i2}, \ldots, w_{ip})$, where $w_{ij} = \Phi^{-1}\{F_{X_j^c}(x_{ij})\}$.

The variation of each of α, β, μ, σ, and δ with distance is characterized using a piecewise linear form consisting of $n_d = 10$ equally spaced nodes over appropriate physical distance domains for the SWNE and NWSE transects. Sensitivity of inference to the choice of n_d near 10 was explored and found to be small. A total of $n_d \times 5 + 2$ parameters need to be estimated.

We optionally also restrict the space of feasible combinations $\{\alpha_j, \beta_j\}, j = 1, 2, \ldots, q$ for each conditioning location to ensure that conditional quantiles from AI models do not exceed those from AD models, as proposed by Keef et al. (2013) (see e.g., Shooter et al., 2019 for further details in a spatial context).

An adaptive MCMC algorithm is used for parameter inference. Briefly, random search is used to find a reasonable starting solution. Then a Metropolis-within-Gibbs algorithm is used iteratively to sample each of the elements of Ω in turn for a total of $n_{\mathrm{MiG}} = 250$ iterations. Subsequently we use the adaptive Metropolis scheme of Roberts and Rosenthal (2009) to jointly update the full set Ω of parameters for a further $n_{\mathrm{GA}} = 50,000$ iterations. Uniform prior distributions on plausible domains are used for model parameters. Chain convergence is judged to have occurred when trace plots for parameters and their dependence stabilize. Fuller description of the MCMC scheme is given in Shooter, Tawn, et al. (2020). MATLAB software, altimeter data and illustrative results are available at Shooter, Ross, and Jonathan (2020).

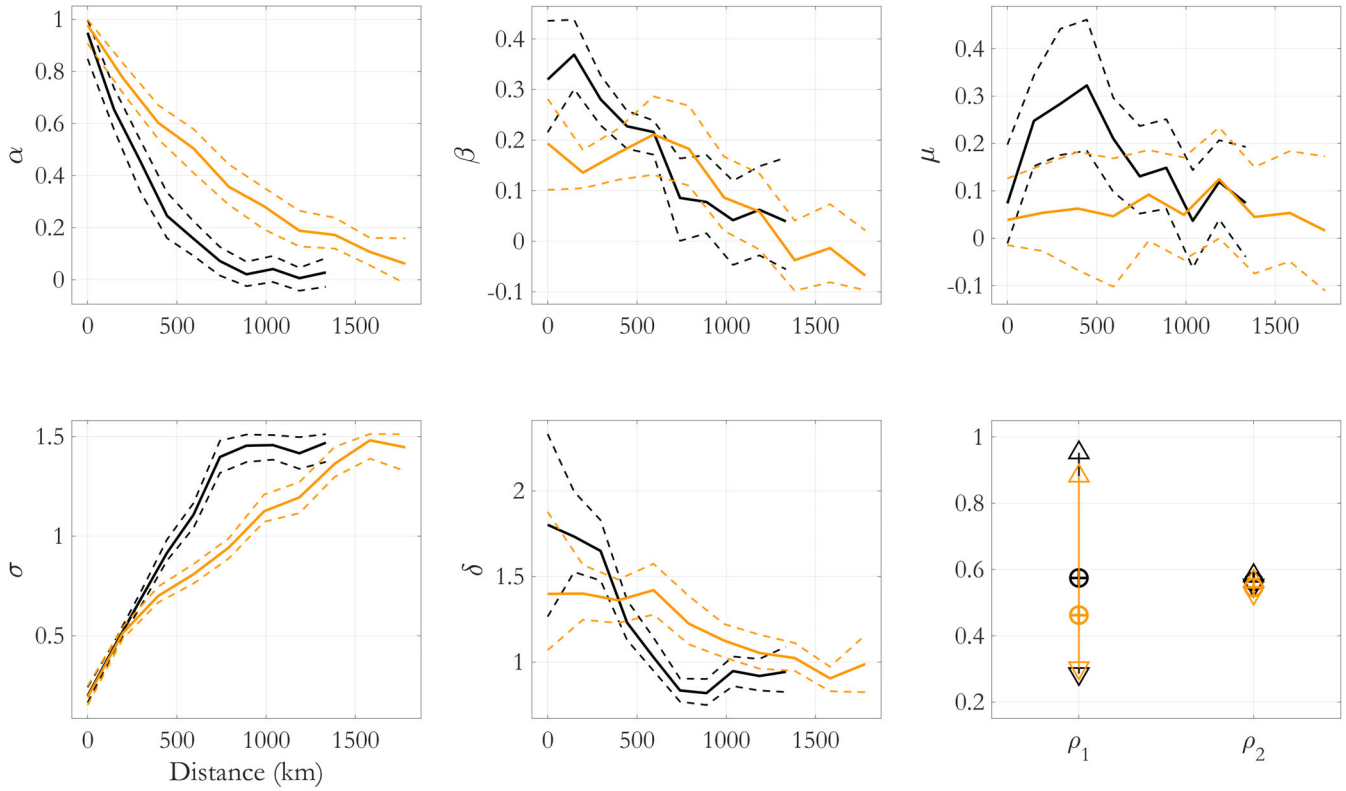

FIGURE 7 Spatial conditional extremes parameter estimates for the normal ascending transect (black) and opposite descending transect (orange) transects, with conditional quantile constraints imposed. Estimates for α, β, μ, σ, and δ as a function of distance (posterior mean and 95% credible interval). Estimates for parameters ρ_1 and ρ_2 in bottom right panel (posterior mean and 95% credible interval)

4 | RESULTS

Parameter estimates for the SCE model estimated for the SWNE and NWSE samples are shown in Figure 7 using a threshold u corresponding to nonexceedance probability 0.7, with the conditional quantile constraints of Keef et al. (2013) imposed. We expect from simple physical considerations, at small distances d, that the characteristics of H_S at the remote location are similar to those at the reference location; in terms of model parameters, this implies $\alpha \approx 1$ and $\beta = \mu = \sigma \approx 0$. At large d, we expect that data from the two locations would correspond to observations from independent standard Laplace distributions, with $\alpha = \mu \approx 0$, $\beta \approx 0$, $\sigma \approx \sqrt{2}$ and $\delta \approx 1$. The parameter estimates found appear to be generally consistent with these expectations. The decay of estimated α with d is greater for the SWNE transect, but this is compensated for by larger estimates for μ at intermediate d. Estimates of β reduce from approximately 0.3 and 0.2 for SWNE and NWSE, to zero with increasing d. Estimates of δ decay from approximately 1.8 and 1.4 to 1.0. The estimated value of σ increases with d from approximately 0.2 to $\sqrt{2}$ for both SWNE and NWSE, but the latter reaches the asymptote sooner after about 700 km. Estimates for parameters ρ_1 and ρ_2 of the conditional Gaussian residual process for SWNE and NWSE are similar.

A number of sensitivity studies were conducted to examine the stability of inferences to different sources of variation; these are reported in Shooter, Ross, and Jonathan (2020). In particular, other threshold choices yield similar parameter estimates and trends with distance. Further, the effect of removing the conditional quantile constraints of Keef et al. (2013) was examined and found to be small, as also noted previously in Shooter, Tawn, et al. (2020). Finally, the effect of changing the conditioning location was examined: general trends observed were consistent with those in Figure 7. To illustrate this specifically, Figure 8 gives estimates for parameters α (top) and σ (bottom) resulting from choosing conditioning locations indexed by 0 (west-most location on transect, see Figure 1), 9 (central location) and 18 (east-most location). Comparing across columns in Figure 8 we see that, regardless of conditioning location, the rate of decay of α with distance for the SWNE transects (black) is greater than for NWSE transects (orange); the same is true for the rate of increase of σ with distance. Note that for conditioning location 9, due its position half way along a transect, we have a smaller range of

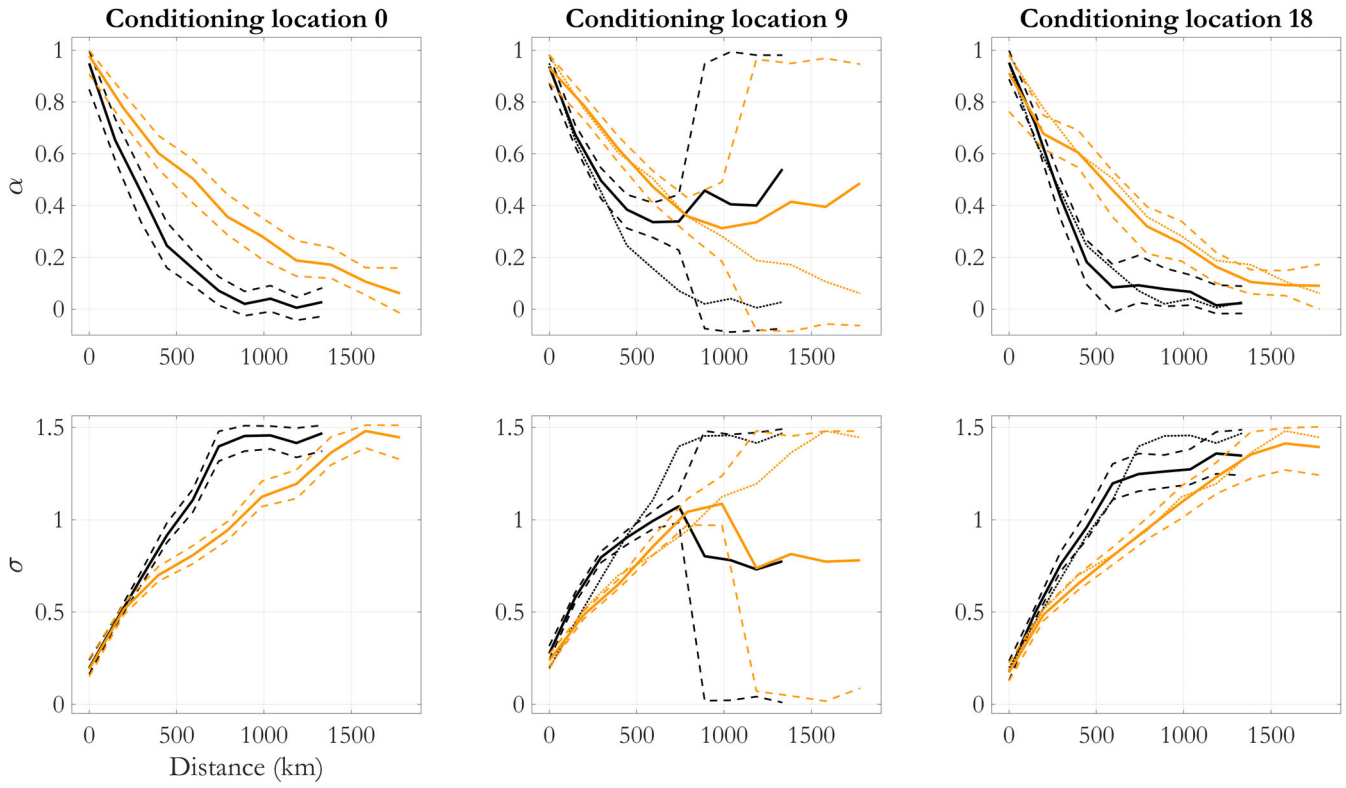

FIGURE 8 Spatial conditional extremes parameter estimates α (top) and σ (bottom) for the normal ascending transect (black) and opposite descending transect (orange) transects, with conditional quantile constraints imposed, for conditioning locations 0 (left), 9 (center), and 18 (right). Estimates are shown as a function of distance (displaying the posterior median and associated 95% credible interval). Dotted lines in the centre and right-hand panels correspond to posterior median profiles for conditioning location 0 for comparison. Illustrations of other parameter estimates are available at Shooter, Ross, and Jonathan (2020)

distances for model fitting, resulting in high parameter uncertainty for large distances (equivalent to the specified prior distribution). Plots for the remaining parameters with distance (see Shooter, Ross, & Jonathan, 2020) do not show such obvious differences between SWNE and NWSE transects.

There is a strong suggestion from Figure 7 that, on the SWNE transect, a remote location at a distance >750 km from the reference location is effectively independent of it since the estimate of α, β, and μ are near zero, the estimate of δ near 1 and the estimate of σ near $\sqrt{2}$. On the NWSE transect, the distance between locations needs to be >1500 km before these conditions are satisfied.

Figure 9 shows the corresponding Laplace-scale conditional mean and SD as a function of distance (see Equation (4)) for the analysis, for conditioning value x_0 with nonexceedance probability 0.9. In terms of conditional mean, the difference between the SWNE and NWSE transect estimates reflects the difference in estimated α parameters. For conditioning quantile with nonexceedance probability 0.7 (not shown), there is little difference between the two conditional mean profiles; in this case, the decay of the SWNE conditional mean with distance takes more of an "S" shape, with slower initial decay and more rapid decay at intermediate distances; the conditional mean decay for the NWSE transect is almost linear. Differences in conditional SDs with distance for conditioning quantile with nonexceedance probability 0.9 (and 0.7) reflect the differences in σ observed in Figure 7.

Figure 10 shows Laplace-scale observations and corresponding trajectories simulated under the fitted models for the SWNE (left) and NWSE transects in terms of five illustrative quantile levels, for conditioning values x_0 corresponding to nonexceedance probabilities $\in (0.7, 0.75]$. There is good agreement between observation and simulation in general.

Figure 11 shows the conditional mean and SD of extreme H_S for SWNE and NWSE transects on the physical scale, assuming that $H_S = 10$ m is observed at the reference location. This is achieved by transforming the corresponding Laplace-scale profiles to physical scale using the estimated generalized Pareto marginal models at each registration location in turn. A value of $H_S = 10$ m corresponds to a nonexceedance probability of approximately 0.98 at the reference location on both transects. There is strong evidence that the conditional mean on the SWNE transect

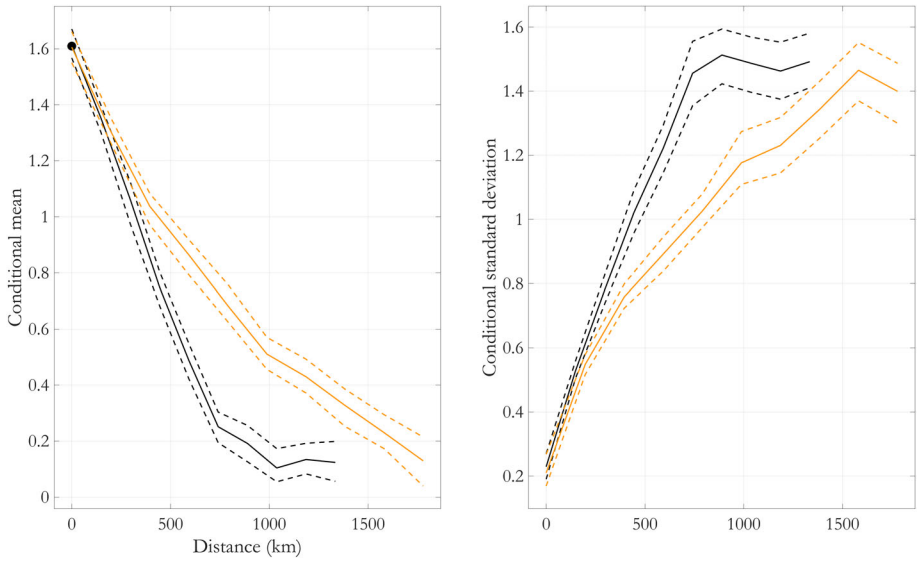

FIGURE 9 Estimates for Laplace-scale conditional mean m and SD s with distance for normal ascending transect (black) and opposite descending transect (orange) transects, with conditional quantile constraints imposed. Conditioning x_0 has nonexceedance probability 0.9. Solid lines represent posterior medians, with dashed lines representing the upper and lower limits of empirical 95% posterior credible intervals

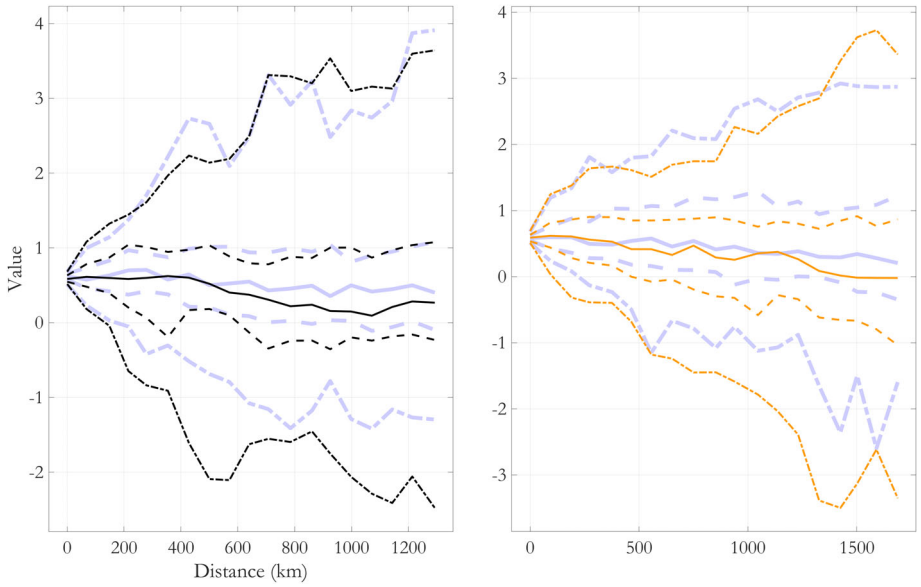

FIGURE 10 Laplace-scale quantiles of observed trajectories (thick blue) and corresponding trajectories simulated under the estimated spatial conditional extremes model with conditional quantile constraints imposed, for normal ascending (black, left) and opposite descending (orange, right) transects. Conditioning values x_0 correspond to nonexceedance probabilities $\in(0.7, 0.75]$. Quantile probabilities shown are 0.025, 0.25, 0.5, 0.75, 0.975

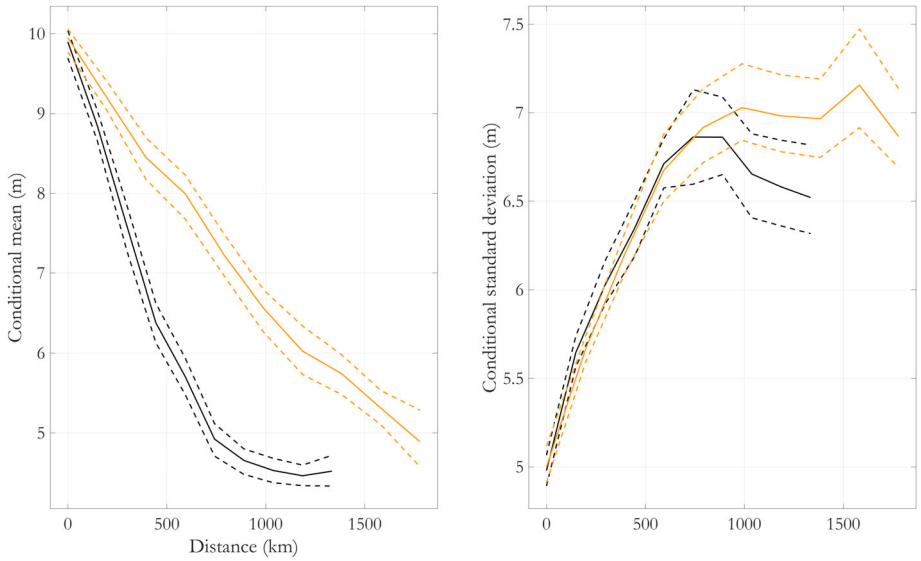

FIGURE 11 Estimates for physical-scale conditional mean m and SD s with distance for normal ascending transect (black) and opposite descending (orange) transects, with conditional quantile constraints imposed. Conditioning value $x_0 = 10$ m corresponds to a nonexceedance probability of approximately 0.98 at the reference location on both transects. Solid lines represent posterior medians, with dashed lines representing the upper and lower limits of empirical 95% posterior credible intervals

decays more quickly than on the NWSE transect, but that the conditional standard deviations are very similar with distance.

Takbash et al. (2019) estimated a generalized Pareto distribution for peaks-over-threshold from a 30-year altimeter record to investigate global values of 100-year return value of H_S. The present results (Figure 4) are consistent in magnitude with estimates from Takbash et al. (2019), yielding slightly higher values in the region of the NWSE compared to the SWNE transect. The NWSE transect is in a relatively more exposed region of the open North Atlantic; Takbash et al. (2019) show that values of 100-year return value for H_S in this region are more uniform along-track than for the SWNE transect. For the SWNE transect, the proximity of Icelandic and UK land masses result in less severe extreme conditions. This may also account for the longer spatial scale (1500 km) determined in the present analysis for the NWSE transect compared to SWNE (750 km).

5 | DISCUSSION AND CONCLUSIONS

In this work we use a SCE model to quantify spatial dependence of extreme values of altimeter measurements of H_S in the North East Atlantic. Combining observations from JASON 1, 2, and 3 for two template transects each consisting of 19 registration locations, we find that model parameters α, β, μ, σ, and δ all vary slowly with distance from a reference location (taken to be the most westerly point on each transect). Parameter estimates for each transect suggest that neighboring locations exhibit near-asymptotic dependence, transitioning to asymptotic independence and eventually full independence with increasing distance. We find strong evidence for differences in extremal spatial characteristics along the transects. For one transect (SWNE) passing from the south-west between the United Kingdom and Iceland, the conditional mean profile given a large value at the south-western reference location decays relatively rapidly with distance; specifically, from 10 m to approximately 5 m over 750 km. For a second transect (NWSE) passing the west coast of Ireland from the north-west, the corresponding decay is more gradual; from 10 m to approximately 5m over 1700 km.

The conditional extremes model requires transformation of observations to standard marginal scale prior to analysis. This is achieved by fitting generalized Pareto models using maximum likelihood estimation at each registration location independently. The estimated marginal models indicate that 100-year return values for H_S exceeding 20 m are to be expected, particularly on the NWSE transect. The conditional extremes model then uses asymptotic arguments to motivate a functional form for the variation of one or more random variables given extreme values of a different conditioning random variable on standard marginal scale. A conditional Gaussian process provides a good representation for residual dependence.

We find that inferences are relatively stable to choice of exceedance threshold for the conditional extremes model, for thresholds with nonexceedance probabilities of at least 0.7. Further we find that imposition of conditional quantile constraints do not materially influence fits. Software, data and illustrations of related sensitivity studies are given at Shooter, Ross, and Jonathan (2020) so that readers can explore the inference further if interested.

The choice of conditioning location for a SCE analysis is in general arbitrary. In this study, a conditioning location was selected at one end of each transect to (a) create a balanced sample for analysis with approximately equal numbers of pairs of observations at any distance and (b) maximize the largest distance available in the sample so that a model for the far field could be estimated as well as possible. We note that, as in Shooter et al. (2019), a pooled analysis could be performed in which a pseudo-likelihood over all possible conditioning locations is adopted. Pooling in this manner complicates the quantification of uncertainty and was not considered here, but is a useful approach, for example, when sample size is small.

Compared with gridded hindcast data, an altimeter samples the ocean surface at a low rate of approximately 10 days relative to the time interval (1–3 days) corresponding to a typical north Atlantic storm. The spatial resolution of altimeter measurements along-track is approximately 10 km. However, the cross-track resolution is low, at approximately 500 km. As a result, some storm events may be under-sampled or missed completely as discussed by Young et al. (2017), Young et al. (2011), Vinoth and Young (2011) and Young et al. (2012). This is a limitation for complete examination of extremes, but may not be problematic in estimation of joint spatial tails of H_S if under-sampling is assumed to occur at random. The quality of altimeter data has been examined in numerous studies, and shown by Ribal and Young (2020) to exhibit smaller random errors than either scatterometer or NDBC buoy data for wind fields. Given these limitations, the process of estimating extreme value models and return values directly from altimeter data is straightforward. Relative to extreme value analysis of hindcast data, the most notable extra task in the current application was to map JASON transects onto

the registration locations on specified SWNE and NWSE template transects of interest, itself the source of some extra variation.

No attempt was made in the current work to account for the effects of covariates (like storm direction and season), which have been found to be influential in marginal extreme value inference (e.g., Feld et al., 2015); a combination of altimeter and scatterometer data sources (e.g., Ribal & Young, 2020) may be exploited to this end. There is also the opportunity to combine altimeter and hindcast data for inference purposes, and to exploit the conditional extremes model of Heffernan and Tawn (2004) directly for joint modeling and calibration of H_S values from multiple sources including in-situ measurements. Jones et al. (2018) illustrate how different sources might be combined for thorough uncertainty quantification.

When there is interest in estimating the joint spatial environmental risk (e.g., along a coastline, or to multiple marine installations, e.g., Kereszturi et al., 2016) from an extreme storm, the spatial conditional extremes model in this work provides a relatively straightforward approach built on established asymptotic results. As illustrated here, altimeter measurements provide a useful high-quality resource for the examination of the spatial structure of wave fields.

ACKNOWLEDGEMENTS

The authors thank two anonymous reviewers and an associate editor for their comments during peer review. The authors also gratefully acknowledge discussions with Matthew Jones, David Randell and Ross Towe (Shell), and Jonathan Tawn (Lancaster University, UK). R. Shooter acknowledges financial support from Shell Research Ltd. and the UK Engineering and Physical Sciences Research Council. I. R. Young acknowledges ongoing financial support from the Integrated Marine Observing System (IMOS) and the Victorian Government through the Department of Environment, Land, Water and Planning, Australia.

DATA AVAILABILITY STATEMENT

MATLAB software and datasets for the analysis are available at Shooter, Ross, and Jonathan (2020).

ORCID

R. Shooter https://orcid.org/0000-0002-2529-0249
E. Ross https://orcid.org/0000-0002-0287-0611
A. Ribal https://orcid.org/0000-0002-3286-5565
I. R. Young https://orcid.org/0000-0003-2233-9227
P. Jonathan https://orcid.org/0000-0001-7651-9181

REFERENCES

Brown, B. M., & Resnick, S. I. (1977). Extreme values of independent stochastic processes. *Journal of Applied Probability*, *14*, 732–739.

Coles, S., Heffernan, J., & Tawn, J. (1999). Dependence measures for extreme value analyses. *Extremes*, *2*, 339–365.

Davison, A. C., Padoan, S. A., & Ribatet, M. (2012). Statistical modelling of spatial extremes. *Statistical Science*, *27*, 161–186.

de Fondeville, R., & Davison, A. C. (2018). High-dimensional peaks-over-threshold inference. *Biometrika*, *105*, 575–592.

Feld, G., Randell, D., Wu, Y., Ewans, K., & Jonathan, P. (2015). Estimation of storm peak and intra-storm directional-seasonal design conditions in the North Sea. *Journal of Offshore Mechanics and Arctic Engineering*, *137*, 021102:1–021102:15.

Ferreira, A., & de Haan, L. (2014). The generalized Pareto process; with a view towards application and simulation. *Bernoulli*, *20*(4), 1717–1737.

Heffernan, J. E., & Resnick, S. I. (2007). Limit laws for random vectors with an extreme component. *The Annals of Applied Probability*, *17*, 537–571.

Heffernan, J. E., & Tawn, J. A. (2004). A conditional approach for multivariate extreme values. *Journal of the Royal Statistical Society: Series B (Statistical Methodology)*, *66*, 497–546.

Huser, R. G., & Wadsworth, J. L. (2019). Modeling spatial processes with unknown extremal dependence class. *Journal of the American Statistical Association*, *114*, 434–444.

Jones, M. J., Hansen, H. F., Zeeberg, A. R., Randell, D., & Jonathan, P. (2018). Uncertainty quantification in estimation of ocean environmental return values. *Coastal Engineering*, *141*, 36–51.

Keef, C., Papastathopoulos, I., & Tawn, J. A. (2013). Estimation of the conditional distribution of a vector variable given that one of its components is large: additional constraints for the Heffernan and Tawn model. *Journal of Multivariate Analysis*, *115*, 396–404.

Kereszturi, M., Tawn, J., & Jonathan, P. (2016). Assessing extremal dependence of North Sea storm severity. *Coastal Engineering*, *118*, 242–259.

Ledford, A. W., & Tawn, J. A. (1996). Statistics for near independence in multivariate extreme values. *Biometrika*, *83*, 169–187.

Reich, B. J., & Shaby, B. A. (2012). A hierarchical max-stable spatial model for extreme precipitation. *The Annals of Applied Statistics*, *6*, 1430–1451.

Ribal, A., & Young, I. R. (2019). 33 years of globally calibrated wave height and wind speed data based on altimeter observations. *Scientific Data*, *6*, 77.

Ribal, A., & Young, I. R. (2020). Global calibration and error estimation of altimeter, scatterometer, and radiometer wind speed using triple collocation. *Remote Sensing*, *12*, 1997.

Ribatet, M. (2013). Spatial extremes: Max-stable processes at work. *Journal de la Société Française de Statistique*, *154*, 156–177.

Roberts, G. O., & Rosenthal, J. S. (2009). Examples of adaptive MCMC. *Journal of Computational and Graphical Statistics*, *18*, 349–367.

Ross, E., Kereszturi, M., van Nee, M., Randell, D., & Jonathan, P. (2017). On the spatial dependence of extreme ocean storm seas. *Ocean Engineering*, *145*, 359–372.

Schlather, M. (2002). Models for stationary max-stable random fields. *Extremes*, *5*, 33–44.

Shooter, R., Ross, E., Jonathan, P., 2020. Spatial conditional extremes for significant wave height from satellite altimetry. Retrieved from https://github.com/ygraigarw/SpatialConditionalExtremesSatellite

Shooter, R., Ross, E., Tawn, J. A., & Jonathan, P. (2019). On spatial conditional extremes for ocean storm severity. *Environmetrics*, *30*, e2562.

Shooter, R., Tawn, J. A., Ross, E., & Jonathan, P. (2020). Basin-wide spatial conditional extremes for severe ocean storms. *Extremes*, 1–25. https://doi.org/10.1007/s10687-020-00389-w

Smith, R. L., 1990. Max-stable processes and spatial extremes. Unpublished manuscript Retrieved from www.stat.unc.edu/postscript/rs/spatex.pdf

Takbash, A., & Young, I. (2019). Global ocean extreme wave heights from spatial ensemble data. *Journal of Climate*, *32*, 6823–6836.

Takbash, A., Young, I., & Breivik, O. (2019). Global wind speed and wave height extremes derived from long-duration satellite records. *Journal of Climate*, *32*, 109–126.

Tawn, J., Shooter, R., Towe, R., & Lamb, R. (2018). Modelling spatial extreme events with environmental applications. *Spatial Statistics*, *28*, 39–58.

Vinoth, J., & Young, I. R. (2011). Global estimates of extreme wind speed and wave height. *Journal of Climate*, *24*, 1647–1665.

Wadsworth, J., & Tawn, J. (2012). Dependence modelling for spatial extremes. *Biometrika*, *99*, 253–272.

Wadsworth, J. L., Tawn, J. A., 2019. Higher-dimensional spatial extremes via single-site conditioning. submission. https://arxiv.org/abs/1912.06560.

Wadsworth, J. L., Tawn, J. A., Davison, A. C., & Elton, D. M. (2017). Modelling across extremal dependence classes. *Journal of the Royal Statistical Society Series C*, *79*, 149–175.

WMO n.d. World meteorological office world weather and climate extremes archive. Highest significant wave height as measured by a buoy. Retrieved from wmo.asu.edu/content/World-Highest-Wave-Buoy

Young, I. (2017). A review of parametric descriptions of tropical cyclone wind-wave generation. *Atmosphere*, *8*, 194.

Young, I. R., & Donelan, M. A. (2018). On the determination of global ocean wind and wave climate from satellite observations. *Remote Sensing of Environment*, *215*, 228–241.

Young, I. R., Sanina, E., & Babanin, A. V. (2017). Calibration and cross validation of a global wind and wave database of altimeter, radiometer, and scatterometer measurements. *The Journal of Atmospheric and Oceanic Technology*, *34*, 1285–1306.

Young, I. R., Vinoth, J., Zieger, S., & Babanin, A. V. (2012). Investigation of trends in extreme value wave height and wind speed. *Journal of Geophysical Research: Oceans*, *117*, C11.

Young, I. R., Zieger, S., & Babanin, A. V. (2011). Global trends in wind speed and wave height. *Science*, *332*, 451–455.

How to cite this article: Shooter R, Ross E, Ribal A, Young IR, Jonathan P. Spatial dependence of extreme seas in the North East Atlantic from satellite altimeter measurements. *Environmetrics*. 2021;e2674. https://doi.org/10.1002/env.2674